Hybrid FMT-MRI applied to *in vivo* atherosclerosis imaging

Baoqiang Li,[1,2] Foued Maafi,[2] Romain Berti,[2] Philippe Pouliot,[1,2] Eric Rhéaume,[2] Jean-Claude Tardif,[2] and Frederic Lesage[1,2,*]

[1]*Institute of Biomedical Engineering, École Polytechnique de Montréal, Montreal, QC, H3C 3A7, Canada*
[2]*Montreal Heart Institute, Montreal, QC, H1T 1C8, Canada*
[*]*frederic.lesage@polymtl.ca*

Abstract: Combining Fluorescent Molecular Tomography (FMT) with anatomical imaging, e.g. MRI facilitates interpreting functional information. Furthermore, using a heterogeneous model for light propagation has been shown in simulations to be superior to homogeneous modeling to quantify fluorescence. Here, we present a combined FMT-MRI system and apply it to heart and aorta molecular imaging, a challenging area due to strong tissue heterogeneity and the presence of air-voids due to lungs. First investigating performance in a phantom and mouse corpse, the MRI-enabled heterogeneous models resulted in an improved quantification of fluorescence reconstructions. The system was then used in mice for *in vivo* atherosclerosis molecular imaging. Results show that, when using the heterogeneous model, reconstructions were in agreement with the *ex vivo* measurements. Therefore, the proposed system might serve as a powerful imaging tool for atherosclerosis in mice.

References and links

1. S. C. Davis, H. Dehghani, J. Wang, S. Jiang, B. W. Pogue, and K. D. Paulsen, "Image-guided diffuse optical fluorescence tomography implemented with Laplacian-type regularization," Opt. Express **15**(7), 4066–4082 (2007).
2. A. Ale, R. B. Schulz, A. Sarantopoulos, and V. Ntziachristos, "Imaging performance of a hybrid x-ray computed tomography-fluorescence molecular tomography system using priors," Med. Phys. **37**(5), 1976–1986 (2010).
3. B. Li, M. Abran, C. Matteau-Pelletier, L. Rouleau, T. Lam, R. Sharma, E. Rhéaume, A. Kakkar, J.-C. Tardif, and F. Lesage, "Low-cost three-dimensional imaging system combining fluorescence and ultrasound," J. Biomed. Opt. **16**(12), 126010 (2011).
4. Y. Lin, W. C. Barber, J. S. Iwanczyk, W. W. Roeck, O. Nalcioglu, and G. Gulsen, "Quantitative fluorescence tomography using a trimodality system: in vivo validation," J. Biomed. Opt. **15**(4), 040503 (2010).
5. B. P. Flynn, A. V. DSouza, S. C. Kanick, S. C. Davis, and B. W. Pogue, "White light-informed optical properties improve ultrasound-guided fluorescence tomography of photoactive protoporphyrin IX," J. Biomed. Opt. **18**(4), 046008 (2013).
6. K. Radrich, A. Ale, V. Ermolayev, and V. Ntziachristos, "Improving limited-projection-angle fluorescence molecular tomography using a co-registered x-ray computed tomography scan," J. Biomed. Opt. **17**(12), 126011 (2012).
7. V. Ntziachristos and R. Weissleder, "Experimental three-dimensional fluorescence reconstruction of diffuse media by use of a normalized Born approximation," Opt. Lett. **26**(12), 893–895 (2001).
8. T. Pyka, R. Schulz, A. Ale, and V. Ntziachristos, "Revisiting the normalized Born approximation: effects of scattering," Opt. Lett. **36**(22), 4329–4331 (2011).
9. J. F. P.-J. Abascal, J. Aguirre, J. Chamorro-Servent, M. Schweiger, S. Arridge, J. Ripoll, J. J. Vaquero, and M. Desco, "Influence of absorption and scattering on the quantification of fluorescence diffuse optical tomography using normalized data," J. Biomed. Opt. **17**(3), 036013 (2012).
10. A. P. Gibson, J. C. Hebden, and S. R. Arridge, "Recent advances in diffuse optical imaging," Phys. Med. Biol. **50**(4), R1–R43 (2005).
11. A. Laidevant, L. Hervé, M. Debourdeau, J. Boutet, N. Grenier, and J.-M. Dinten, "Fluorescence time-resolved imaging system embedded in an ultrasound prostate probe," Biomed. Opt. Express **2**(1), 194–206 (2011).

12. J. Boutet, L. Herve, M. Debourdeau, L. Guyon, P. Peltie, J. M. Dinten, L. Saroul, F. Duboeuf, and D. Vray, "Bimodal ultrasound and fluorescence approach for prostate cancer diagnosis," J. Biomed. Opt. **14**(6), 064001 (2009).
13. A. Ale, V. Ermolayev, E. Herzog, C. Cohrs, M. H. de Angelis, and V. Ntziachristos, "FMT-XCT: in vivo animal studies with hybrid fluorescence molecular tomography-X-ray computed tomography," Nat. Methods **9**(6), 615–620 (2012).
14. A. Ale, V. Ermolayev, N. C. Deliolanis, and V. Ntziachristos, "Fluorescence background subtraction technique for hybrid fluorescence molecular tomography/x-ray computed tomography imaging of a mouse model of early stage lung cancer," J. Biomed. Opt. **18**(5), 056006 (2013).
15. D. E. Sosnovik, M. Nahrendorf, N. Deliolanis, M. Novikov, E. Aikawa, L. Josephson, A. Rosenzweig, R. Weissleder, and V. Ntziachristos, "Fluorescence tomography and magnetic resonance imaging of myocardial macrophage infiltration in infarcted myocardium in vivo," Circulation **115**(11), 1384–1391 (2007).
16. J.-C. Tardif, F. Lesage, F. Harel, P. Romeo, and J. Pressacco, "Imaging biomarkers in atherosclerosis trials," Circ Cardiovasc Imaging **4**(3), 319–333 (2011).
17. F. A. Jaffer, P. Libby, and R. Weissleder, "Optical and multimodality molecular imaging: insights into atherosclerosis," Arterioscler. Thromb. Vasc. Biol. **29**(7), 1017–1024 (2009).
18. S. C. Davis, B. W. Pogue, R. Springett, C. Leussler, P. Mazurkewitz, S. B. Tuttle, S. L. Gibbs-Strauss, S. S. Jiang, H. Dehghani, and K. D. Paulsen, "Magnetic resonance-coupled fluorescence tomography scanner for molecular imaging of tissue," Rev. Sci. Instrum. **79**(6), 064302 (2008).
19. Y. Lin, M. T. Ghijsen, H. Gao, N. Liu, O. Nalcioglu, and G. Gulsen, "A photo-multiplier tube-based hybrid MRI and frequency domain fluorescence tomography system for small animal imaging," Phys. Med. Biol. **56**(15), 4731–4747 (2011).
20. C. M. Carpenter, R. Rakow-Penner, S. Jiang, B. L. Daniel, B. W. Pogue, G. H. Glover, and K. D. Paulsen, "Inspired gas-induced vascular change in tumors with magnetic-resonance-guided near-infrared imaging: human breast pilot study," J. Biomed. Opt. **15**(3), 036026 (2010).
21. J. Sanz and Z. A. Fayad, "Imaging of atherosclerotic cardiovascular disease," Nature **451**(7181), 953–957 (2008).
22. D. A. Sanan, D. L. Newland, R. Tao, S. Marcovina, J. Wang, V. Mooser, R. E. Hammer, and H. H. Hobbs, "Low density lipoprotein receptor-negative mice expressing human apolipoprotein B-100 develop complex atherosclerotic lesions on a chow diet: no accentuation by apolipoprotein(a)," Proc. Natl. Acad. Sci. U.S.A. **95**(8), 4544–4549 (1998).
23. Q. Fang and D. A. Boas, "Monte Carlo simulation of photon migration in 3D turbid media accelerated by graphics processing units," Opt. Express **17**(22), 20178–20190 (2009).
24. J. Yuan, E. Bae, and X.-C. Tai, "A study on continuous max-flow and min-cut approaches," in 2010 IEEE Conference on Computer Vision and Pattern Recognition (CVPR), 2217–2224 (2010).
25. G. Alexandrakis, F. R. Rannou, and A. F. Chatziioannou, "Tomographic bioluminescence imaging by use of a combined optical-PET (OPET) system: a computer simulation feasibility study," Phys. Med. Biol. **50**(17), 4225–4241 (2005).
26. S. A. Prahl, "Online resource: http://omlc.ogi.edu/spectra".
27. P. K. Yalavarthy, B. W. Pogue, H. Dehghani, and K. D. Paulsen, "Weight-matrix structured regularization provides optimal generalized least-squares estimate in diffuse optical tomography," Med. Phys. **34**(6), 2085–2098 (2007).
28. P. C. Hansen and D. P. O'Leary, "The use of the L-curve in the regularization of discrete ill-posed problems," SIAM J. Sci. Comput. **14**(6), 1487–1503 (1993).
29. V. S. Talanov, C. A. S. Regino, H. Kobayashi, M. Bernardo, P. L. Choyke, and M. W. Brechbiel, "Dendrimer-based nanoprobe for dual modality magnetic resonance and fluorescence imaging," Nano Lett. **6**(7), 1459–1463 (2006).
30. F. Gao, H. Zhao, and Y. Yamada, "Improvement of image quality in diffuse optical tomography by use of full time-resolved data," Appl. Opt. **41**(4), 778–791 (2002).
31. F. Leblond, K. M. Tichauer, R. W. Holt, F. El-Ghussein, and B. W. Pogue, "Toward whole-body optical imaging of rats using single-photon counting fluorescence tomography," Opt. Lett. **36**(19), 3723–3725 (2011).

1. Introduction

One of the advantages of combining fluorescence molecular tomography (FMT) with anatomical imaging is anatomical guidance for an improved quantification of reconstructions [1–6]. While previous reports show that Born-normalization could cancel off some experimental factors, such as laser coupling loss, camera gain and exposing time, as well as reduce the effect of absorption heterogeneity in fluorescence reconstructions [7]; but limitations to suppress scattering variations were found [8]. Furthermore, it was demonstrated in simulations that homogeneous forward models might induce significant quantification errors in the reconstruction, which could be improved by propagating light in a heterogeneous model [9]. In this context, especially working with continuous wave (CW) mode, in which

absorption and scattering cannot be separated [10], anatomical imaging is an essential addition in order to optimize forward modeling and achieve an accurate reconstruction.

Hybrid modality imaging combining FMT with MRI, X-ray CT, or ultrasound has been increasingly used in human breast, prostate and preclinical cancer models [11–14]. However, cardiovascular imaging in small animals has mostly been limited to *ex vivo* or *in vitro* imaging [15] due to the high absorption of light by the heart [16], the presence of air gaps due to lungs and the heterogeneous nature of light absorption properties of tissue in this region. Furthermore, the aorta, which is often a target in atherosclerosis imaging [17], has a relatively small size leading to challenges both for optical detection and structural delineation. Nevertheless noninvasive *in vivo* imaging plays an important role in preclinical atherosclerosis studies [17]. Therefore, combining the high sensitivity of FMT with the high spatial resolution of MRI, a hybrid FMT-MRI system is expected to improve *in vivo* atherosclerosis imaging in small animals.

The objectives of this study were threefold: (1) To develop a novel hybrid modality FMT-MRI system to explore both functional information and anatomy simultaneously; (2) to evaluate the benefits of using a heterogeneous model of tissues for light propagation [9]; and (3) to provide a proof of concept for *in vivo* atherosclerosis imaging of mice. To achieve these objectives, we developed a fiber-based optical probe to acquire conduct FMT in parallel with MRI. By addressing source fibers sequentially with a Galvo mirror and detecting using a single snapshot of all the detection fibers with a sensitive electron multiplying charge coupled device (EMCCD) camera, our system enabled faster optical sampling than the existing FMT-MRI systems [18–20]. The system was next characterized with a phantom and then with a mouse corpse containing a known fluorescent inclusion, thereby demonstrating quantification improvements when using heterogeneous modeling. Finally, the system was used to image matrix metalloproteinase (MMP) activity, an important target for atherosclerosis imaging [17, 21] in atherosclerotic (ATX) and control (Ctrl) mice [22].

2. System

2.1 FMT system design

As shown in Fig. 1, a collimated laser beam at 660 nm (HL6545MG, Thorlabs) was first cleaned up by a band-pass filter (FF01-661/11, Semrock), and then re-directed by a galvo mirror (GVS012, Thorlabs), to be focused by two lenses (LA1257-B, Thorlabs) towards an optical fiber matrix (FT200UMT, Thorlabs). A total of 36 fibers were used for excitation, positioned in a matrix covering a 15 mm × 15 mm area. Similarly, 36 fibers were employed for detection. The detection fibers were mounted on a metal plate, and filmed by a sensitive EMCCD camera (Nüvü Cameras).

The received light corresponding to different detection fibers was thus collected by distinct pixels of the EMCCD chip. The camera exposition time was set to 100 milliseconds for all imaging presented in this work. Detection wavelength was selected by optical filters mounted on a motorized filter wheel (FW103, Thorlabs). In this study, the emitted fluorescence was selected by a band-pass filter, FF01-716/40 (Semrock) optimized for Cy5.5. To reach the MRI bore, each fiber was 6 m long, and connected to a home-made MRI-compatible optical probe. Light coupling loss was measured to be around 40% on average. Components were synchronized by a data acquisition (DAQ) card (NI USB-6353, NI).
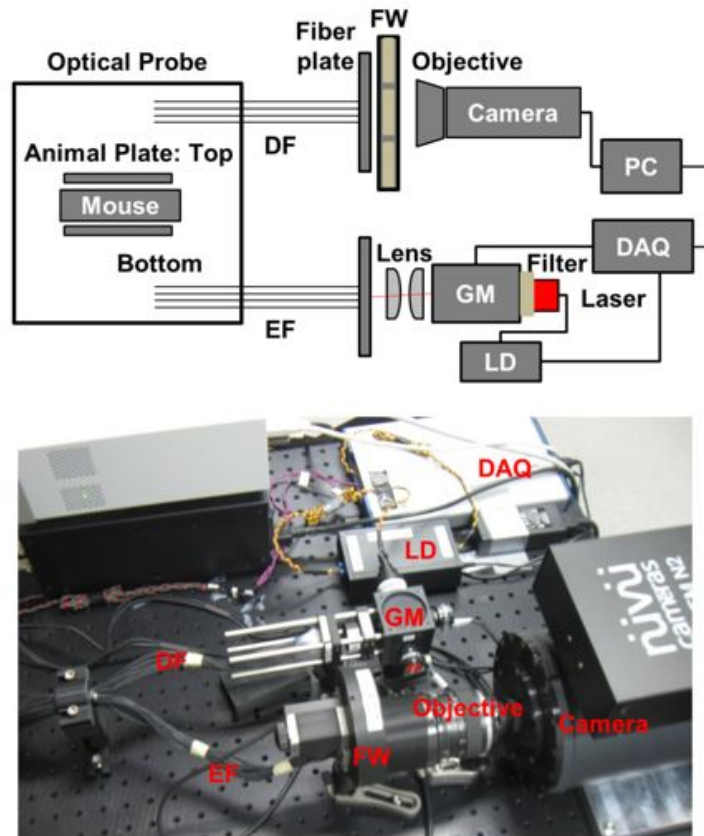
Fig. 1. Schematic (top) and photograph (bottom) of the FMT system. GM: Galvo mirror; EF: excitation fibers; DF: detection fibers; LD: laser driver; FW: Filter wheel.

2.2 Optical probe design

The optical probe consisted of two MRI compatible plastic plates (animal plates). The top one is illustrated by the schematic diagram in Fig. 2. This plate was mounted with 18 excitation fibers and 18 detection fibers interlaced with a distance of 3 mm and covering a total area of 15 mm × 15 mm. Likewise, the same geometry was employed for the bottom (not shown). As seen in the photograph, the animal was installed between the two plates with the region of interest (ROI) covered by the fibers. The distance between the two plates could be adjusted to allow the fibers to be brought into close contact with the sample. Each fiber was protected by a black rubber shrink-tube to prevent contamination from ambient light and to reduce crosstalk between fibers. Five holes, serving as fiducial markers, were made on the plate (Fig. 2). By filling with water prior to MR imaging, the holes could be visualized in MR images and used as reference to localize fibers for the simulation of photon propagation for each source. The photograph in Fig. 2 shows how the optical probe was installed on the MRI animal holder. With this planar setup, both transmission and reflection measurements were obtained from two sides of the animal. But only transmission data was used for reconstruction. A 7-Tesla MRI system with 30 cm bore (Agilent) was used in this study. As previously mentioned, MRI and fluorescence imaging were done simultaneously.
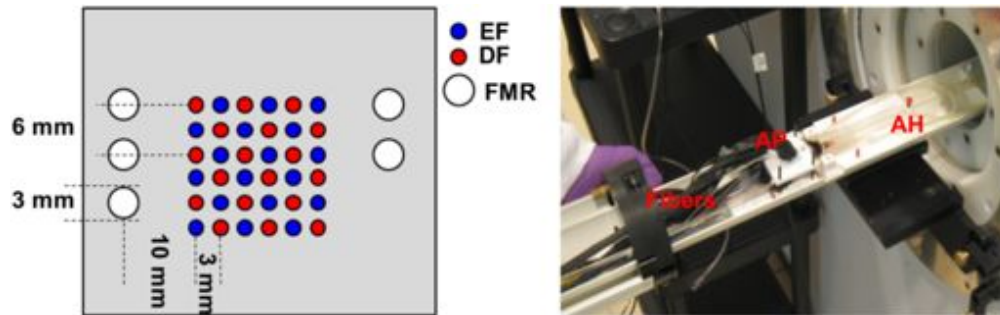
Fig. 2. Schematic diagram (left, top side) and photograph (right) of the optical probe working in an experiment. AH: animal holder; AP: animal plate; FMR: fiducial marker.

3. Reconstruction

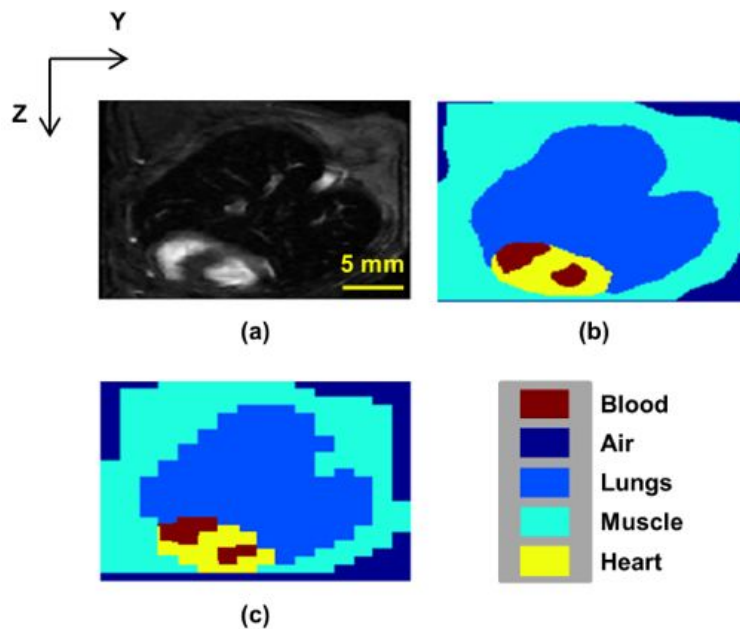### 3.1 MR anatomy guided forward modeling

Fig. 3. (a) Representative axial MR slice of ATX #2; (b) segmented image; (c) resampled segmented image with 1 mm voxel resolution.

Photons propagation was simulated using Monte-Carlo simulations on GPU [23]. To define tissue boundaries for heterogeneous photon propagation, a fast segmentation algorithm was used [24] supplemented by manual correction. The segmentation process is shown in a representative slice of one mouse (ATX #2 below). As shown by the MR slice in Fig. 3(a), blood was bright with this sequence so that the heart and aorta could easily be segmented. The rest of the body was automatically separated into air, lungs, blood and muscle. The boundaries between different sections were manually corrected for all the slices. Lung walls could not be separated, and were regarded as muscle for photon propagation. Lung cavities were set to air in forward modeling. The segmented image by this semi-automatic method is shown in Fig. 3(b). The image was resampled to 1 mm voxel resolution for forward modeling (Fig. 3(c)). Literature optical properties were assigned according to the segmentation [25, 26].

This semi-automatic segmentation was also used in the experiment with the mouse corpse (images not shown). In that experiment, fat tissue was brighter in the MR images; and the

fluorescent inclusions were approximately inserted into the liver area of the mouse corpse, where the heart and lungs were not included in the FOV of FMT. Because the biological composition was different from a living mouse and the organs were delocalized due to inserting fluorescence inclusions, the corpse was simply segmented to muscle and fat.

3.2 MR-prior constrained reconstruction

Image reconstruction was done by minimizing the following objective function:

$$\Omega = \left\| \Phi^{meas} - W\chi \right\|^2 + \lambda \left\| L\chi \right\|^2, \tag{1}$$

Where $\lambda \left\| L\chi \right\|^2$ is a penalty term to regularize the reconstruction process and reduce its ill-posedness. Then, the first-order condition, $\dfrac{\partial \Omega}{\partial \chi} = 0$, leads to the following iterative minimization process, as detailed in Ref [27]:

$$\chi_{i+1} = [W^T W + \lambda L^T L]^{-1} W^T (\Phi_i^{meas} - \Phi_i^C) + \chi_i, \tag{2}$$

where

$$W = \frac{\int_V G^x(r_s, r) G^m(r, r_d) d^3 r}{G^x(r_s, r_d)}. \tag{3}$$

Here, $\mathbf{\Phi}^{meas}$ and $\mathbf{\Phi}^C$ are the experimental and simulated Born ratios [7]; W is the sensitivity matrix; χ represents the fluorescence yield εηC, in which ε, η and C are the extinction coefficient, quantum yield and concentration of the fluorophore. The matrix L encodes the prior localization of fluorescence emission in Laplacian form; it is used to constrain reconstruction as a soft-prior [27]. λ is the regularization parameter to adjust the strength of the penalty term; $G^x(r_s, r)$ and $G^m(r, r_d)$ are two Green functions, which describe the photon propagations from source (r_s) to an arbitrary position in tissue (r), and from tissue to detector (r_d), respectively. Finally, reconstruction was performed iteratively, and i represents the iteration index. Convergence was said to be achieved when the projection error between two iterations was below 1%. However, a maximum of eight iterations was imposed to avoid the estimated error increasing [27].

To diminish the error in reconstruction induced by an imprecise segmentation and/or an inadequate knowledge on the localization of fluorescence emission, the matrix L encoding spatial priors was used only in the first iteration but replaced by an identity matrix in the following iterations. The initial value of fluorescent yield was set to be zero. It has been reported that an optimal λ was often determined empirically [27]. But to avoid bias on this part, the initial value of λ was determined by an L-curve method [28]. As a result, the value of λ was less than 2 for all the reconstructions presented in this study.

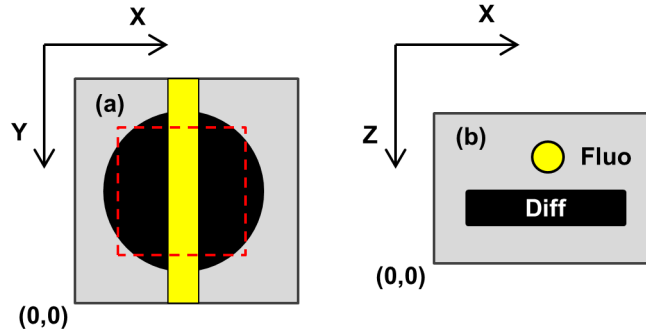## 4. Experiments

4.1 Phantom experiment

Fig. 4. Schematic diagram of the phantom: (a) view of X-Y plane; (b) view of X-Z plane. The attenuation and fluorescence inclusions are denoted by Diff and Fluo, respectively.

Table 1. Dimension and optical properties of the phantom.

	Center position (mm)			Dimension (mm)				Optical properties (mm^{-1})	
	X	Y	Z	Diameter	X	Y	Z	μ_α	$\mu_s^{'}$
Bulk	–	–	–	–	30	30	20	0.02	1.0
Diff	13	15	7	18	–	–	6	0.005	0.5
Fluo	14	–	13	4	–	30	–	–	–

Phantom experiments were first conducted to characterize the FMT system and the associated reconstruction algorithm. The dimension of the phantom is illustrated in Fig. 4 with detailed information provided in Table 1. The phantom was installed between the two plates with the fibers covering an area approximately illustrated by the dashed red square in Fig. 4(a). Cylindrical transparent tubes (length: 30mm, inner ⌀: 3mm) filled with Cy5.5 solution at concentrations of 200nM, 100nM and 50nM were inserted into 'Fluo' in Fig. 4(b), and then imaged. For confirmation and to account for potential dilution errors, each fluorescent tube was imaged *ex vivo* using a commercial epi-illumination fluorescence imaging system (IVIS Lumina, PerkinElmer).

4.2 Mouse corpse experiment

To mimic the *in vivo* environment, a mouse corpse was employed to evaluate the FMT-MRI system. Transparent tubes, of each having a volume of ~106μL, filled with Cy5.5 solution at 600nM and 400nM were each inserted into approximately the same region in the body and then imaged by the FMT-MRI system. For MRI imaging, a T1-weighted 3D sequence was used so that fatty tissue was bright. Parameters were TR/TE = 5.0, 2.5 ms, FA = 30, matrix size of 256 x 192 x 256, 4 averages, 16 minutes scan time. Spatial resolution along the X, Y and Z direction was 0.18 mm, 0.16 mm and 0.16 mm (Fig. 7). The whole FMT-MRI process took ~20 minutes for each concentration.

4.3 In vivo experiment

The FMT-MRI system was then used to evaluate *in vivo* molecular imaging of atherosclerosis. All animal manipulations were approved by the ethics committee of Montreal Heart Institute. Two ATX (LDLR$^{-/-}$; Human Tg (apoB$^{+/+}$); ~19 months old) and two Ctrl (C57/B6; ~3 months old) mice were imaged, labeled ATX #1, #2 and Ctrl #1, #2 in the following. The ATX mice have a gene deletion in the LDL receptor (*Ldlr*) gene and overexpress the human apolipoprotein B. Mice lacking the LDL receptor will develop atherosclerosis spontaneously without the need of high fat diet during 16 weeks [22].

Using those mice at advanced age (19 months) allow them to develop a severe atherosclerotic plaque on a chow diet, in which the metalloproteinase's (MMP's) activity would be higher compared to the wild type mice (C57/B6). To visualize MMPs activity induced by atherosclerosis, ~16 nmol of a molecular probe (MMPSense 680, PerkinElmer) was intravenously administered, with the dose being proportional to the individual weight. For each mouse, imaging was conducted before and 24 hours after the administration of the probe. For FMT, the field of view (FOV) of the optical probe was designed to approximately cover the heart area. For MRI, a 2D CINE bright blood sequence (in rapid single phase mode) was used with cardiac but no respiratory gating. The parameters were as follows: TR in the range 120-140 ms (one R-R interval), TE = 1.8 ms, FA = 30, 256 x 256 matrix leading to 0.18 x 0.14 mm resolution (see Fig. 8), 30 slices of 1 mm thickness, 20 averages. For each mouse, the FMT-MRI process was completed in ~45 minutes. After the experiment, the mice were sacrificed and dissected; hearts and aortas were imaged *ex vivo* for evaluation.
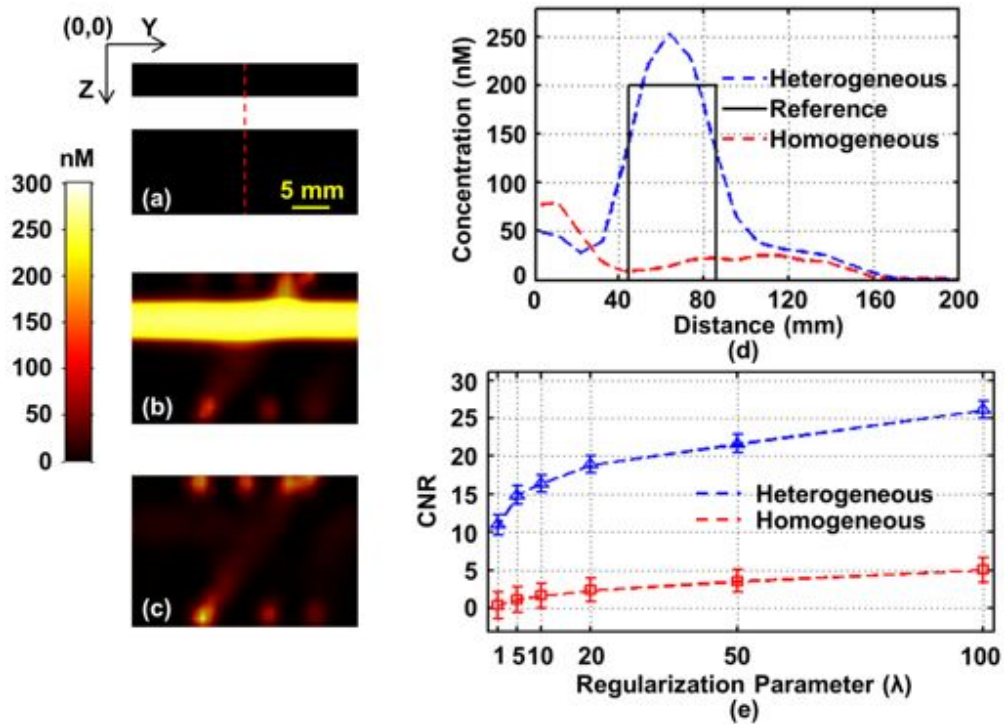
5. Results

5.1 Phantom experiment

Fig. 5. (a) A synthetic fluorescence slice of the phantom; (b) the corresponding slices of the reconstruction with the heterogeneous models (b), and with the homogeneous model (c), respectively; (d) plot of reconstructed values along the red dashed line. (e) CNR was compared with λ for both models.

Phantom experiments were used to evaluate the impact of heterogeneous modeling on the quantification of fluorescence reconstructions. A heterogeneous model was built as illustrated in Fig. 4, with optical properties assigned according to Table 1. The homogeneous model used bulk optical properties to propagate light. In both models, the fluorescent inclusion, denoted by 'Fluo' in Fig. 4(b), was assigned with the bulk optical properties. Identical optical properties were assumed at the excitation and the emission wavelengths consistent with small absorption changes expected with this phantom. Finally, the localization of the tubes was

used as a soft-prior to constrain the reconstructions of the fluorescence yield $\varepsilon\eta C$. Taking the published values of ε and η [29], concentration C of the embedded Cy5.5 fluorophore was then estimated. As shown in Fig. 5, a representative reconstruction of the fluorescent tube filled with 200nM Cy5.5 solution. One slice of the phantom is illustrated in Fig. 5(a), with the fluorescent tube indicated by the white bar. The reconstructed concentration of the corresponding slice with the heterogeneous and homogeneous models is presented in Figs. 5(b)-5(c). As shown, heterogeneous modeling resulted in better localization and quantification. The reconstructed concentration values along the red dashed line in Fig. 5(a) were plotted for analysis (Fig. 5(d)). Overall, the reconstructed concentrations of the fluorescent inclusions with the heterogeneous models for 200nM, 100nM and 50nM were estimated at ~260nM, ~151nM and ~83nM, respectively. Contrast to Noise Ratio was also evaluated as defined by CNR = $(S_A-S_B)/\sigma$, where S_A/S_B is the average value of the fluorescent inclusion/background respectively, σ is the standard deviation of background. With heterogeneous reconstructions, the CNRs were 11.6, 11.7 and 10.7 for the cases of 200nM, 100nM and 50nM, respectively. With the homogeneous models, the CNRs were ~29 times lower on average. Shown in Fig. 5(e), different λ from 1 to 100 were used in the reconstructions. The homogeneous reconstructions were significantly improved with greater λ. And a better CNR could be consistently achieved with heterogeneous model for each λ.
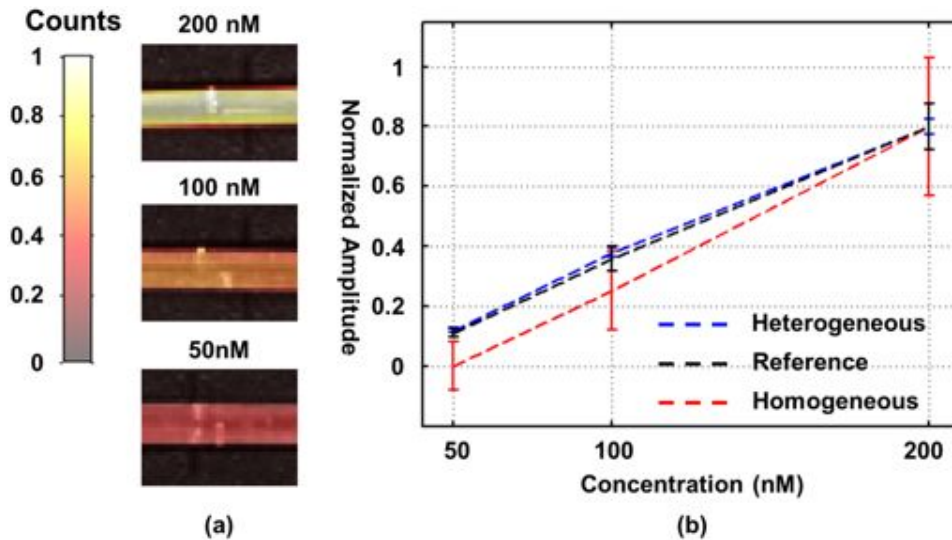

Fig. 6. (a) *Ex vivo* images of the fluorescent tubes were overlaid with transparency (alpha = 0.5) on the photographs of tubes, respectively; (b) the average reconstructed values (both models) of the fluorescent tubes were normalized of the maximum being 1, to compare with the *ex vivo* measurement (reference).

In Fig. 6(a), the fluorescent tubes were measured *ex vivo* as reference; and the fluorescence images were overlaid with transparency (alpha = 0.5) on the photographs of the tubes. Then, the average reconstructed values in the fluorescent inclusions for different cases of concentrations were normalized to the maximum. As shown in Fig. 6(b), linearity was achieved for the reconstructions with both heterogeneous and homogeneous models. Nonetheless, the heterogeneous model reconstructions show a higher fidelity to the reference. When quantified, the standard deviation of the difference between the reconstruction with the heterogeneous model and the reference is ~0.01; but, drops to ~0.06 for the homogeneous counterpart.
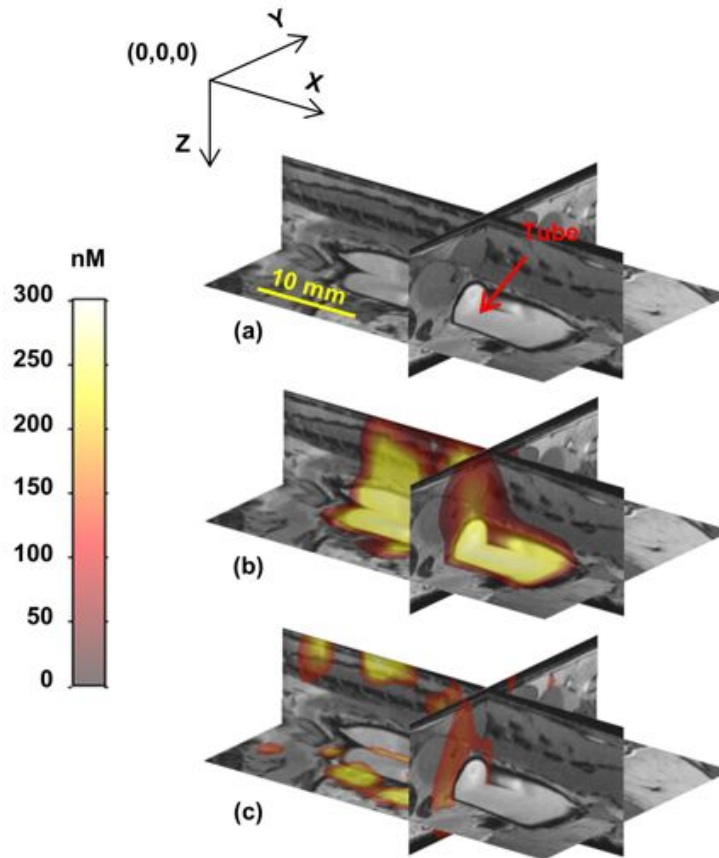
5.2 Mouse corpse experiment

Fig. 7. (a) Three orthogonal MR slices are shown: axial slice (Y-Z), coronal slice (X-Y) and sagittal slice (X-Z). The arrow of the X axes points to tail of the mouse; and the arrow of the Z axes points to abdomen. The tube was indicated by the red arrow; (b) the reconstructions with the heterogeneous models were overlaid with transparency (alpha = 0.5) on the MR slices, respectively; (c) the reconstructions with the homogeneous models were overlaid with transparency (alpha = 0.5) on the MR slices, respectively.

Results obtained with the fluorescent tube filled with 400nM Cy5.5 solution are presented as an example. Three orthogonal MR slices are shown in Fig. 7(a). For visualization, the reconstructed images were overlaid with transparency (alpha = 0.5) on the MR slices and a threshold was set to reduce background intensities. With this experiment, the reconstructed concentrations with the heterogeneous model for the cases of 600nM and 400nM were ~640nM and ~237nM with CNRs of ~7.7 and ~2.7, respectively. Again, the CNR of the reconstructions with the heterogeneous models were ~6.6 times better than their homogeneous counterpart. Linearity was compared for the reconstructions with both types of models and the standard deviation of the difference between the heterogeneous reconstructions and the reference was ~0.22, but dropped to ~0.89 for the homogeneous counterpart.

Both CNR and linearity of the reconstructions decreased when compared to the phantom experiment likely due to greater absorption and scattering of tissue, which deteriorated SNR of the corresponding measurements. The value of regularization parameter, determined by the L-curve method, was estimated lower in this case which may reduce reconstruction contrast

[27]. Finally, although taking into account the heterogeneity of the mouse corpse, the forward modeling remained a considerable approximation due to the rough segmentation.
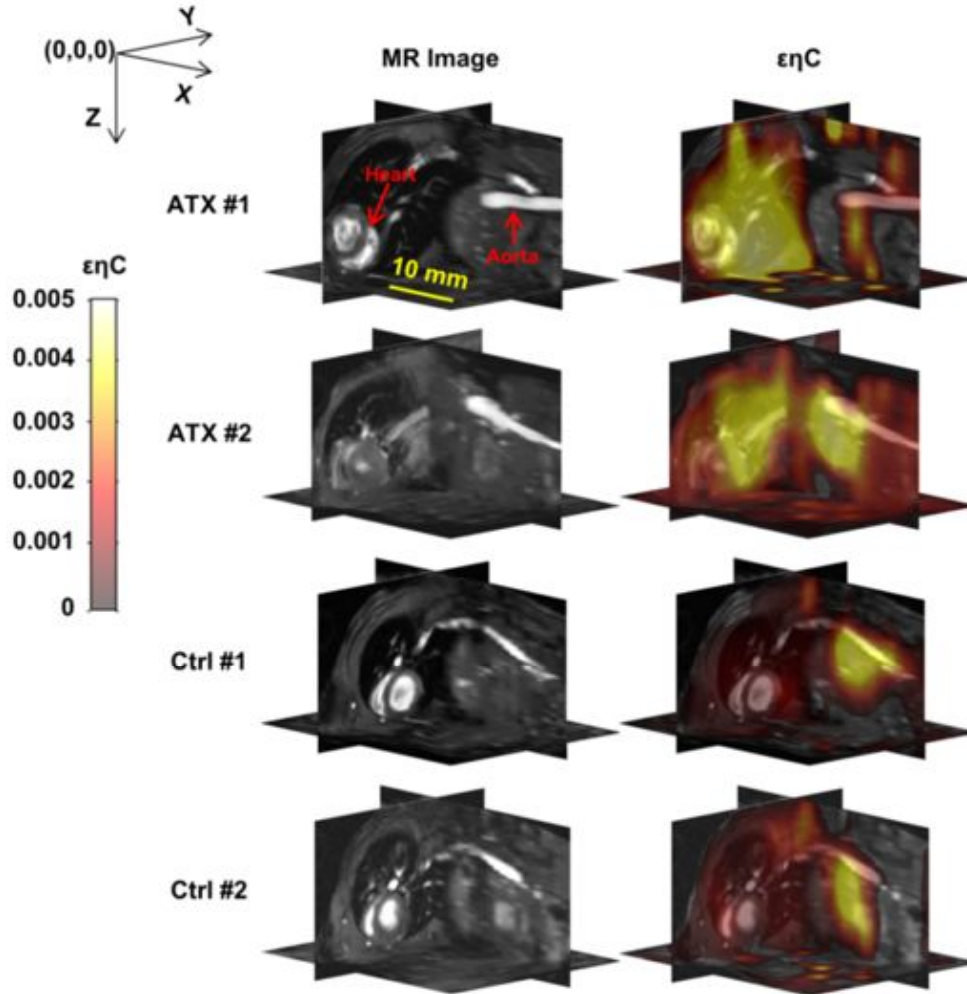
5.3 In vivo experiment

Fig. 8. The images in the first column are the MR slices for each mouse. Heart and part of aorta of ATX #1 were denoted by red arrows. In the second column, the reconstructed εηC with the heterogeneous models were overlaid with transparency (alpha = 0.5) on the MR slices, respectively. Three orthogonal MR slices were chosen for each mouse: axial slice (Y-Z), coronal slice (X-Y) and sagittal slice (X-Z).

Finally, the reconstructions of the four mice are shown in Fig. 8. Because the values of ε and η are unknown for this molecular probe, fluorescence yield $\varepsilon\eta C$ instead of concentration is presented. As identified a posteriori by the *ex vivo* analysis, a considerable amount of fluorescence signal was observed in the lungs. Therefore, the heart, aorta and lungs were used as soft-prior to constrain the reconstructions. MR image slices used for segmentation are shown in the first column of Fig. 8. Here, the axial slice is approximately located in the center of the heart while the sagittal slice was chosen to visualize part of the descending aorta. In the second column of Fig. 8, the reconstructed $\varepsilon\eta C$ with the heterogeneous model is overlaid with transparency (alpha = 0.5) on the corresponding MR slices. For visualization, a threshold was set to reduce background intensities. Fluorescence intensity was higher in the ATX mice than

the control ones, which might reflect the known increase MMPs activity of the ATX mice. The average value of $\varepsilon\eta C$ on the regions of heart and aorta for ATX #1, ATX #2, Ctrl #1 and Ctrl #2 was ~0.0027, ~0.0024, ~0.0011 and ~0.0011, respectively. As with the dead mouse experiment, reconstructions with the homogeneous models were underestimated (data not shown).
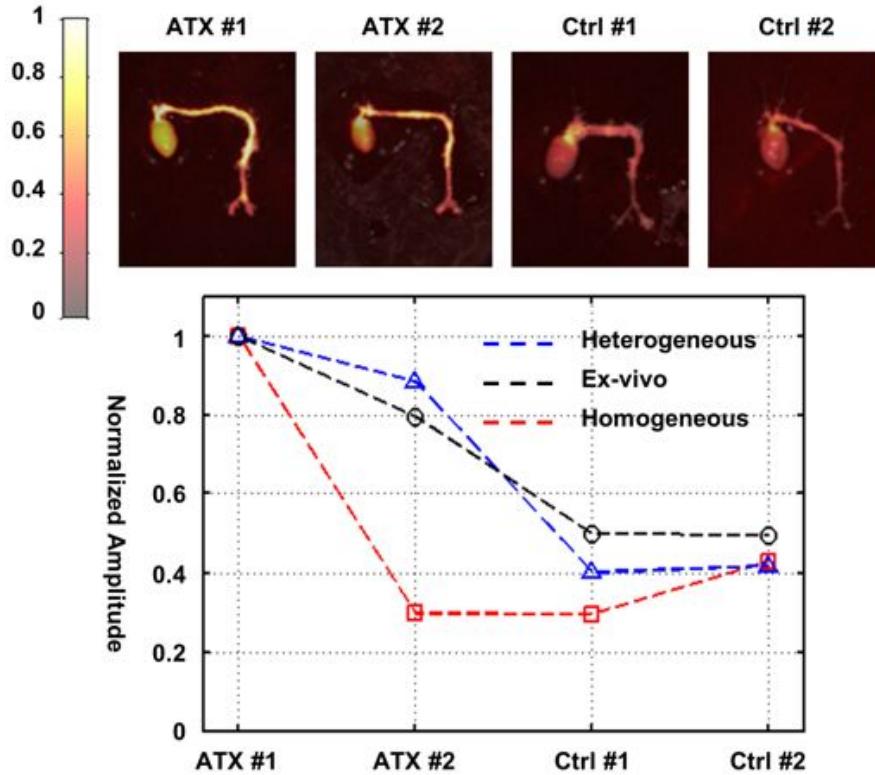

Fig. 9. The hearts and aortas of the four mice were imaged *ex vivo*. In the first row, the *ex vivo* fluorescence images were overlaid with transparency (alpha = 0.5) on the corresponding photographs. Shown by the curves below, the average reconstructed $\varepsilon\eta C$ of the hearts and aortas for all mice were normalized with the maximum being 1 to compare with the *ex vivo* measurement.

Reconstructions were then evaluated by *ex vivo* measurements (Fig. 9). In the first row, fluorescence from the heart and aorta is shown for all mice confirming increase uptake in ATX #1 and #2. A comparison of reconstruction estimations with *ex vivo* measurements is also provided for both homogeneous and heterogeneous forward modeling (normalized to ATX #1). Quantitatively, the standard deviation of the difference between the reconstructions with the heterogeneous models and the *ex vivo* measurement was ~0.08, but drops to ~0.22 for the homogeneous counterpart.

6. Discussion

In this paper, a hybrid-modal FMT-MRI system targeted to mouse cardiovascular imaging was presented. Working with long fibers, emitted photons corresponding to all detection fibers for each source could be recorded in one single snapshot with an EMCCD camera. Hence, a full measurement at one wavelength for all sources (36) was completed within ~30 seconds. An optical probe was designed to quickly install the animal within the MRI holder. Therefore, with fibers on the top and bottom sides of the optical probe, transmission measures

were obtained from both sides of the animal; and MRI was conducted simultaneously to FMT.

One of the objectives of this study was to achieve an improved quantification of reconstructions with heterogeneous forward modeling. MR-anatomy enabled the construction of a heterogeneous model for improved simulations of photons propagation, including void regions created by lungs. To evaluate benefits of this approach, reconstructions with both heterogeneous and homogeneous models were compared using experimental measures on phantoms. The results confirm that heterogeneous modeling is beneficial to reconstructions both in terms of localization and quantification. There results were further confirmed using a more realistic geometry using a mouse corpse.

Finally, the FMT-MRI system was applied in *in vivo* imaging of atherosclerosis. Following administration of a molecular probe, specific fluorescence signal was detected, which reflects the MMPs activity involved in the progression of atherosclerosis. With the heterogeneous models, the evaluation of fluorescence yield from the hearts and aortas were well correlated to the *ex vivo* measurements, not as clearly with homogenous modeling.

There remain limitations to this study: besides forward modeling, anatomical prior information could also benefit the inverse problem which was not investigated here. Second, although taking into account the heterogeneity of tissue, rough segmentations of the MR anatomies and the use of literature values for optical properties might induce modeling error. Time-resolved measurements may provide some help [30] to reconstruct first the optical properties. Finally, we showed that a soft-prior could help obtain better quantitative reconstructions. Nonetheless, such priors are not always achievable in *in vivo* experimental situations. In this study, although heart and aorta are the major targets for atherosclerosis imaging, MMPs activated fluorescence was found more broadly from the body of mice. Lungs were found to have considerable fluorescence and thus included in the priors. However, to avoid over-constrain, the soft-priors were only used in the first iteration of reconstruction and replaced with an identity matrix for the following iterations. Alternatively, it might be expected that with an optimized forward model and a more advanced detection mechanism [31] having better SNR, the reliance of prior on reconstruction could be alleviated.

7. Conclusion

In summary, we have developed a hybrid-modal FMT-MRI system to explore both functional and anatomical information in mice. Using MR-derived anatomical information, the benefits of heterogeneous forward modeling was demonstrated in experiments encompassing phantom, mouse corpse and *in vivo* imaging of atherosclerosis. The reconstructions with the heterogeneous models showed higher fidelity to the *ex vivo* measurements when compared to the homogeneous model. Therefore, the proposed FMT-MRI system associated with the reconstruction method might serve as a tool for atherosclerosis imaging of small animals. Furthermore, due to its improved acquisition rate, the future application of this system will be in dual-modality pharmacokinetic imaging with preclinical tumorous mice.

Acknowledgments